This is a repository copy of *Uncovering s-shaped IV curves in organic photovoltaics: The role of DIO-driven vertical segregation*.

White Rose Research Online URL for this paper:
https://eprints.whiterose.ac.uk/id/eprint/227461/

Version: Accepted Version

Article:

Spooner, E.L.K. orcid.org/0000-0001-9575-550X, Kilbride, R.C. orcid.org/0000-0002-3985-923X, Cai, J. et al. (9 more authors) (2025) Uncovering s-shaped IV curves in organic photovoltaics: The role of DIO-driven vertical segregation. ACS Applied Materials & Interfaces. ISSN 1944-8244

https://doi.org/10.1021/acsami.5c04713

© 2025 The Authors. Except as otherwise noted, this author-accepted version of a journal article published in ACS Applied Materials & Interfaces is made available via the University of Sheffield Research Publications and Copyright Policy under the terms of the Creative Commons Attribution 4.0 International License (CC-BY 4.0), which permits unrestricted use, distribution and reproduction in any medium, provided the original work is properly cited. To view a copy of this licence, visit http://creativecommons.org/licenses/by/4.0/

Reuse

This article is distributed under the terms of the Creative Commons Attribution (CC BY) licence. This licence allows you to distribute, remix, tweak, and build upon the work, even commercially, as long as you credit the authors for the original work. More information and the full terms of the licence here: https://creativecommons.org/licenses/

Takedown

If you consider content in White Rose Research Online to be in breach of UK law, please notify us by emailing eprints@whiterose.ac.uk including the URL of the record and the reason for the withdrawal request.

eprints@whiterose.ac.uk
https://eprints.whiterose.ac.uk/

Uncovering S-Shaped IV Curves in Organic Photovoltaics: The Role of DIO-Driven Vertical Segregation

Emma L. K. Spooner[1,2†], Rachel C. Kilbride[1,3,4†*], Jinlong Cai[5,6], Kaicheng Shi[7], Roderick MacKenzie[8], Elena J. Cassella[1], Philipp Gutfreund[9], Russell J. Holmes[7], Tao Wang[5,6], Richard Jones[10], David G. Lidzey[1] and Andrew J. Parnell[1]***

1. School of Mathematics and Physical Sciences, The University of Sheffield, Hicks Building, Hounsfield Road, Sheffield, S3 7RH, United Kingdom
2. The Photon Science Institute, The University of Manchester, Oxford Road, Manchester, M13 9PY, United Kingdom
3. Department of Physics, The University of Warwick, Coventry, CV4 7AL, United Kingdom
4. XMaS, The UK Materials Science Facility, European Synchrotron Radiation Facility, F-38043 Grenoble, France
5. School of Materials Science and Engineering, Wuhan University of Technology, Wuhan 430070, China
6. School of Materials and Microelectronics, Wuhan University of Technology, Wuhan 430070, China
7. Department of Chemical Engineering and Materials Science, University of Minnesota, Minneapolis, Minnesota 55455, United States
8. Department of Engineering, Durham University, Lower Mount Joy, South Road, Durham DH1 3LE, United Kingdom
9. Institut Laue-Langevin, 71 avenue des Martyrs, CS 20156, 38042 Grenoble, France
10. Department of Materials, The University of Manchester, Sackville Street Building Manchester, M1 3BB, United Kingdom

*Corresponding authors: emma.spooner@manchester.ac.uk, rachel.kilbride@warwick.ac.uk, a.j.parnell@sheffield.ac.uk

†These authors contributed equally to this work

Keywords: Organic photovoltaics, stability, morphology, bulk heterojunction, solvent additives, vertical segregation

Abstract

Controlling vertical segregation in organic photovoltaics (OPV) is critical for achieving optimal solar cell performance and stability, requiring careful consideration of a range of factors such as the surface energy and miscibility of components, solvent and solvent additive identity, and film processing methods. In this work, we use neutron reflectivity to compare vertical segregation in two different OPV systems: a fullerene-based system (PBDB-T:$PC_{71}BM$) and a non-fullerene-based system (PBDB-T:ITIC), processed with different amounts of the solvent additive, 1,8-diiodooctane (DIO). Both systems exhibit vertical segregation, with enrichment of the acceptor at the film/hole transport layer interface. However, segregation is considerably more pronounced in ITIC-based systems, where the enriched interface consists of pure ITIC, compared to a maximum of 67% $PC_{71}BM$ by volume in the former system. Prolonging film drying with higher solvent additive content exacerbates segregation in both systems, increasing interfacial acceptor concentration in $PC_{71}BM$ systems and broadening the buried interface in ITIC systems. Simulations confirm that extreme vertical segregation in ITIC-based devices induces non-ideal ‘s-shaped’ JV curves when the enriched layer is pure and sufficiently thick, as seen in both fresh and aged devices. Our findings highlight that improper vertical segregation not only leads to poor device performance in fresh devices, but gradual segregation can also contribute to morphological degradation and device instabilities over time.

1. Introduction

Organic photovoltaics (OPVs) are an emerging thin film solar technology, offering tunable absorption, lightweight and flexible design and compatibility with low-temperature, large-area roll-to-roll manufacture.[1] These advantages make OPVs well-suited for a versatile range of applications including building-integrated PV, portable electronics, indoor PV and autonomous Internet of Things devices.[2,3] With the development of non-fullerene acceptors (NFAs), the power conversion efficiency (PCE) of OPVs has recently surpassed 20%.[4,5] However, despite these impressive efficiencies, OPVs are susceptible to degradation from both intrinsic and extrinsic factors, limiting their operational stability, and therefore restricting commercial efforts thus far.[6]

Achieving optimal OPV performance and stability relies on careful control of the morphology of the bulk heterojunction (BHJ) blend film. Key morphological parameters – donor and acceptor domain size, crystallinity, domain purity, interconnectivity and vertical distribution – each play crucial roles in determining the efficiency of exciton dissociation, charge transport and charge extraction.[7] In particular, the vertical distribution of the blend components in the plane perpendicular to the electrodes directly impacts vertical charge transport and extraction at the film/electrode interface.[8,9] Furthermore, whilst it has been demonstrated that morphological changes such as increased phase-separation and crystallinity can occur over time,[10] evolution of the vertical distribution in blend films and its implications for device stability is yet to be fully understood.

Vertical segregation in OPV films can arise due to a range of factors relating to both intrinsic material properties such as surface energy, miscibility and molecular structure,[8,9] as well as film processing conditions such as thermal annealing, solvent annealing and the addition of solvent additives.[11–13] Solvent additives, such as 1,8-diiodooctane (DIO) and 1-chloronaphthalene, are typically used to prolong film drying,[14] often yielding purer phases and enhanced phase separation. They can also be employed to favorably control vertical segregation,[11,15] through selective component solubility[16] or changes in the drying time.[17]

Various techniques including dynamic secondary ion mass spectroscopy,[8,18] X-ray photoelectron spectroscopy (XPS),[19] near edge X-ray absorption fine structure spectroscopy (NEXAFS),[20] spectroscopic ellipsometry (SE),[21] X-ray reflectivity[22] and neutron reflectivity (NR) have been employed to characterize vertical segregation in blend films.[23] NR in particular has proven highly effective for characterizing the vertical component distribution in polymer:fullerene systems, benefitting from the non-destructive and high penetrative nature of neutrons, as well as the significant intrinsic neutron scattering length density (SLD) contrast between fullerenes (SLD ~ 4.5×10^{-6} Å^{-2}) and polymers (SLD ~ 1.0×10^{-6} Å^{-2}).[24-28] More recently, NR has been applied to polymer:NFA systems;[17,29-31] however, these systems typically exhibit considerably lower SLD contrasts due to the similar chemical structure of NFAs and typical donor polymers, limiting the effectiveness of the technique. Deuteration of one component has been demonstrated as a successful method to enhance SLD contrast between polymers and NFAs, offering a route to characterizing the morphology of polymer:NFA systems using neutron scattering techniques.[32-34]

Vertical segregation of donor and acceptor components in a BHJ can have favorable or unfavorable consequences, depending on the energetic alignment of the accumulated component and its adjacent charge transport layer. Extreme vertical segregation can yield barriers to charge transport, and result in kinked or 's-shaped' JV curves. For example, Tress *et al.* noted that imbalanced mobilities, combined with vertical phase separation induced BHJ inhomogeneity which could create s-shaped curves.[35] Similarly, Love *et al.*[15] and Finck *et al.*[36] have linked s-shaped curves to improper vertical distribution within a BHJ, which in the former case was improved through the addition of a solvent additive.

In other works, s-shaped JV curves have been attributed to injection or extraction barriers;[37,38] imbalanced mobilities between donor and acceptor;[39] finite surface recombination velocities;[40] and charge carrier traps.[41] The first of these has itself been linked to unmatched work functions of the nonoptimized charge transport layers, especially those requiring UV light activation;[42] electrode oxidation;[43] and improper layer thicknesses.[44]

In this work, we explore the relationship between vertical segregation, device *JV* curve characteristics, and device stability using two common OPV systems, namely the combination of donor polymer poly[(2,6-(4,8-bis(5-(2-ethylhexyl)thiophen-2-yl)-benzo[1,2-b:4,5-b']dithiophene))-alt-(5,5-(1',3'-di-2-thienyl-5',7'-bis(2-ethylhexyl)benzo[1',2'-c:4',5'-c']dithiophene-4,8-dione)] (**PBDB-T**) with a fullerene acceptor [6,6]-Phenyl-C_{71}-butyric acid methyl ester (**PC$_{71}$BM**) or NFA 3,9-bis(2-methylene-(3-(1,1-dicyanomethylene)-indanone))-5,5,11,11-tetrakis(4-hexylphenyl)-dithieno[2,3-d:2',3'-d']-s-indaceno[1,2-b:5,6b']dithiophene (**ITIC**). Vertical segregation in these systems is characterized using neutron reflectometry (NR). To overcome the limited SLD contrast in PBDB-T:ITIC blend films, we synthesize a deuterated ITIC analogue (ITIC-d_8). In PBDB-T:PC$_{71}$BM systems, there is sufficient intrinsic SLD contrast between the polymer and fullerene components such that deuteration is not necessary.

Our results show that processing with DIO significantly impacts the *JV* curve behavior of the two systems with PBDB-T:ITIC systems exhibiting non-ideal, 's-shaped' curves in both fresh and aged devices processed with high amounts of DIO. Using NR and drift-diffusion simulations we show that DIO-mediated vertical segregation is the primary cause of the observed s-shaped behavior with considerable consequences on the performance and long-term stability of OPV devices.

2. Results and Discussion

2.1 Device Performance

The two OPV systems were first compared via fabrication of conventional architecture devices, using the structure ITO/PEDOT:PSS/Active Layer/PFN-Br/Ag. The full experimental details can be found in the **Experimental Methods**. Molecular structures of the active layer materials can be found in **Figure 1a**, alongside their UV-Visible absorption in **Figure 1b** (PBDB-T:ITIC) and **1c** (PBDB-T:$PC_{71}BM$).

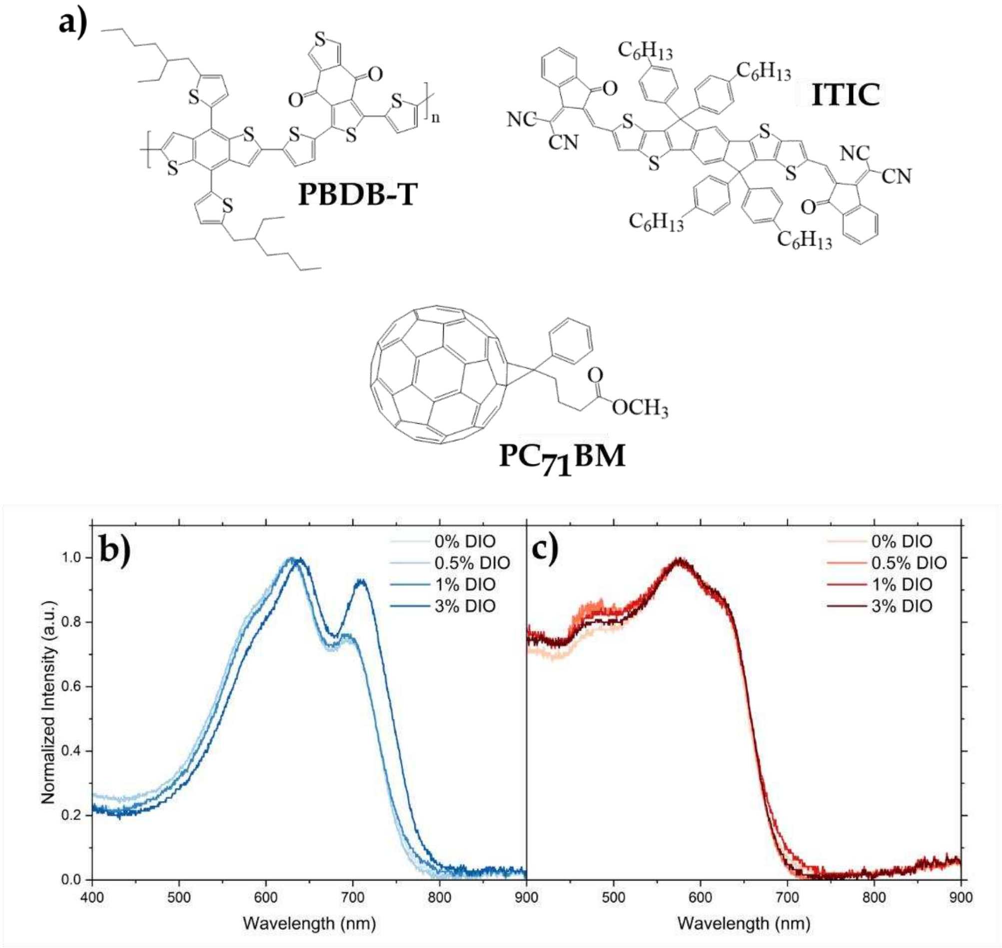

Figure 1: ***a)*** *Chemical structures of the donor and acceptors used, UV-Visible absorption of the* ***b)*** *PBDB-T:ITIC and* ***c)*** *PBDB-T:$PC_{71}BM$ blend films with varying amounts of added DIO.*

Box plots comparing PBDB-T:ITIC and PBDB-T:$PC_{71}BM$ devices with a range of DIO volume concentrations, alongside their *JV* curves, can be found in **Figure 2**. Device metrics are also summarized in **Table 1**.

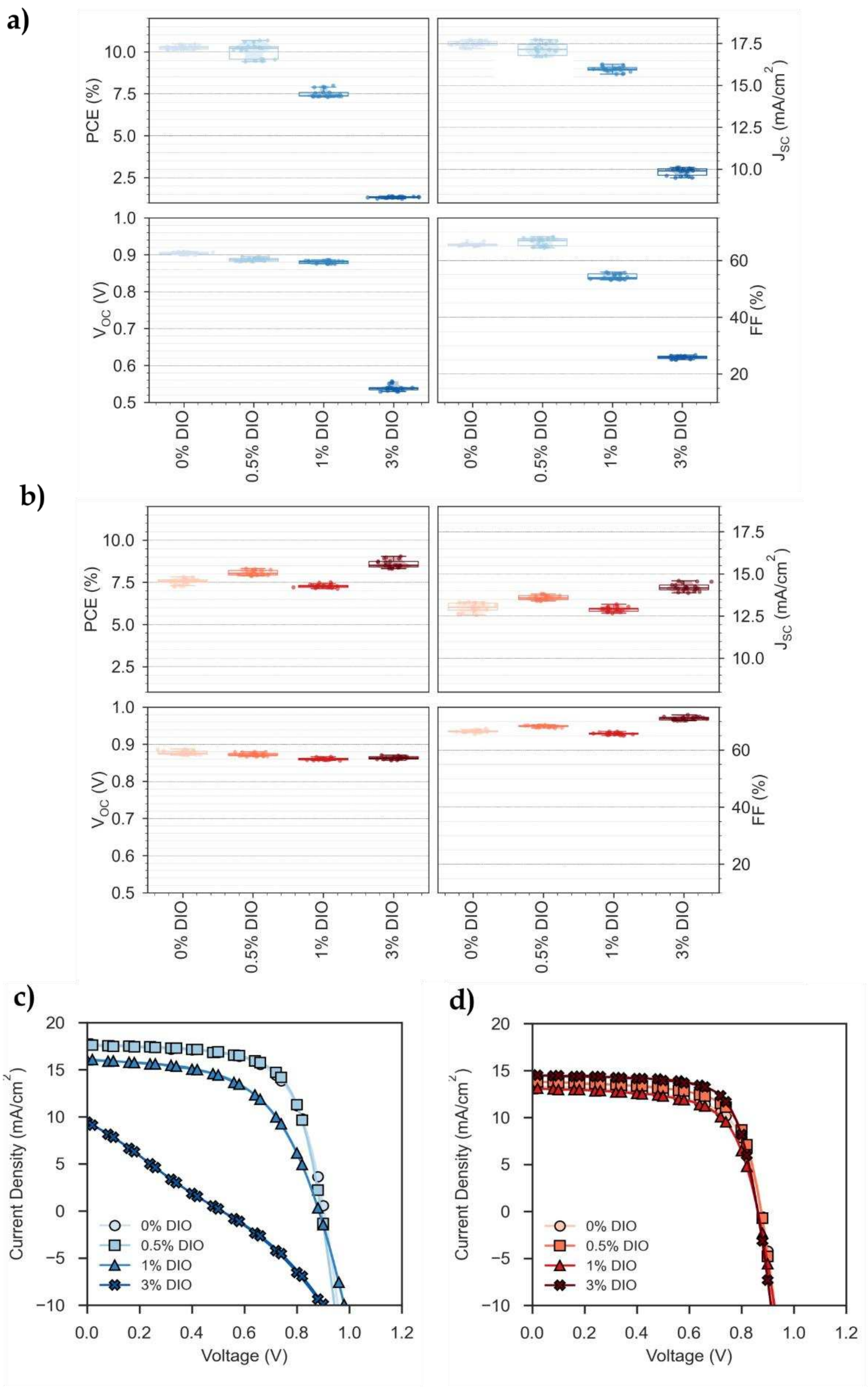

Figure 2: *Box plots showing device metrics for* ***a)*** *PBDB-T:ITIC and* ***b)*** *PBDB-T:PC$_{71}$BM based OPVs. 10 devices shown for each concentration of DIO. Boxplot characteristics: bottom whisker = first quartile – interquartile range, bottom of the box = first quartile, central line = median, top of the box = third quartile, top whisker = third quartile + interquartile range. Champion device J-V sweeps shown for* ***c)*** *PBDB-T:ITIC and* ***d)*** *PBDB-T:PC$_{71}$BM.*

Table 1: *Summary of device metrics for PBDB-T:ITIC and PBDB-T:PC$_{71}$BM based OPVs. All metrics are given as the average of 10 devices ± 1 standard deviation, with the champion value shown in brackets.*

Active layer	DIO Concentration (%)	J_{sc} (mA cm^{-2})	V_{oc} (V)	FF (%)	PCE (%)
PBDB-T:ITIC	0	17.5 ± 0.17 (**17.7**)	0.90 ± 0.003 (**0.91**)	65.6 ± 0.49 (**66.9**)	10.3 ± 0.12 (**10.5**)
	0.5	17.1 ± 0.44 (**17.7**)	0.89 ± 0.005 (**0.90**)	66.5 ± 1.30 (**68.4**)	10.1 ± 0.42 (**10.7**)
	1	16.0 ± 0.88 (**16.3**)	0.88 ± 0.004 (**0.89**)	54.3 ± 0.94 (**55.9**)	7.5 ± 0.22 (**8.0**)
	3	9.9 ± 0.21 (**10.1**)	0.54 ± 0.008 (**0.56**)	25.8 ± 0.52 (**26.7**)	1.3 ± 0.04 (**1.4**)
PBDB-T:PC$_{71}$BM	0	13.0 ± 0.25 (**13.3**)	0.88 ± 0.005 (**0.89**)	66.6 ± 0.39 (**67.5**)	7.5 ± 0.16 (**7.8**)
	0.5	13.6 ± 0.14 (**13.8**)	0.87 ± 0.004 (**0.88**)	68.3 ± 0.32 (**68.8**)	8.1 ± 0.15 (**8.3**)
	1	12.9 ± 0.13 (**13.2**)	0.86 ± 0.003 (**0.87**)	65.7 ± 0.40 (**66.5**)	7.3 ± 0.10 (**7.5**)
	3	14.2 ± 0.21 (**14.6**)	0.86 ± 0.004 (**0.87**)	71.1 ± 0.57 (**72.3**)	8.6 ± 0.22 (**9.0**)

As expected, without solvent additive addition the PBDB-T:ITIC based devices outperform those based on PBDB-T:PC$_{71}$BM, due to the superior absorption and charge transport properties of the NFA. Upon addition of DIO, champion performance marginally increases for PBDB-T:ITIC, before dropping sharply at concentrations of 1% and above. The relationship between DIO concentration and PBDB-T:PC$_{71}$BM performance is less clear, but in general higher additive amounts yield superior performance.

The decrease in device performance upon increasing DIO content for PBDB-T:ITIC based cells is reflected in all device metrics- with reductions in short circuit current density (J_{SC}), open circuit voltage (V_{OC}) and fill factor (FF), reflecting the catastrophic breakdown in function. Other studies[45] have linked poor PBDB-T:ITIC device performance with high concentrations of DIO, and its role in promoting excessive ITIC crystallization. Here we highlight the non-ideal 's-shaped' *JV* curve for the addition of 3% DIO, possibly implying the formation of a charge extraction or a charge injection barrier.

2.2 Device stability

To explore how these s-shaped *JV* curves evolve over time, the devices were aged in the dark, and in an inert atmosphere. Removal of extrinsic degradation factors such as moisture and oxygen, should confine changes in device performance to intrinsic factors, for example morphological evolution of the active layer, or reactions between components in the cell. Evolution of the PCE over time can be seen in **Figure 3a**, with further metrics given in **Figures S1a - d**. The changes in the *JV* curves for PBDB-T:ITIC based devices with 1% and 3% of DIO can be seen in **Figure 3b** and **3c,** with those for other devices shown in **Figures S2 – 3**.

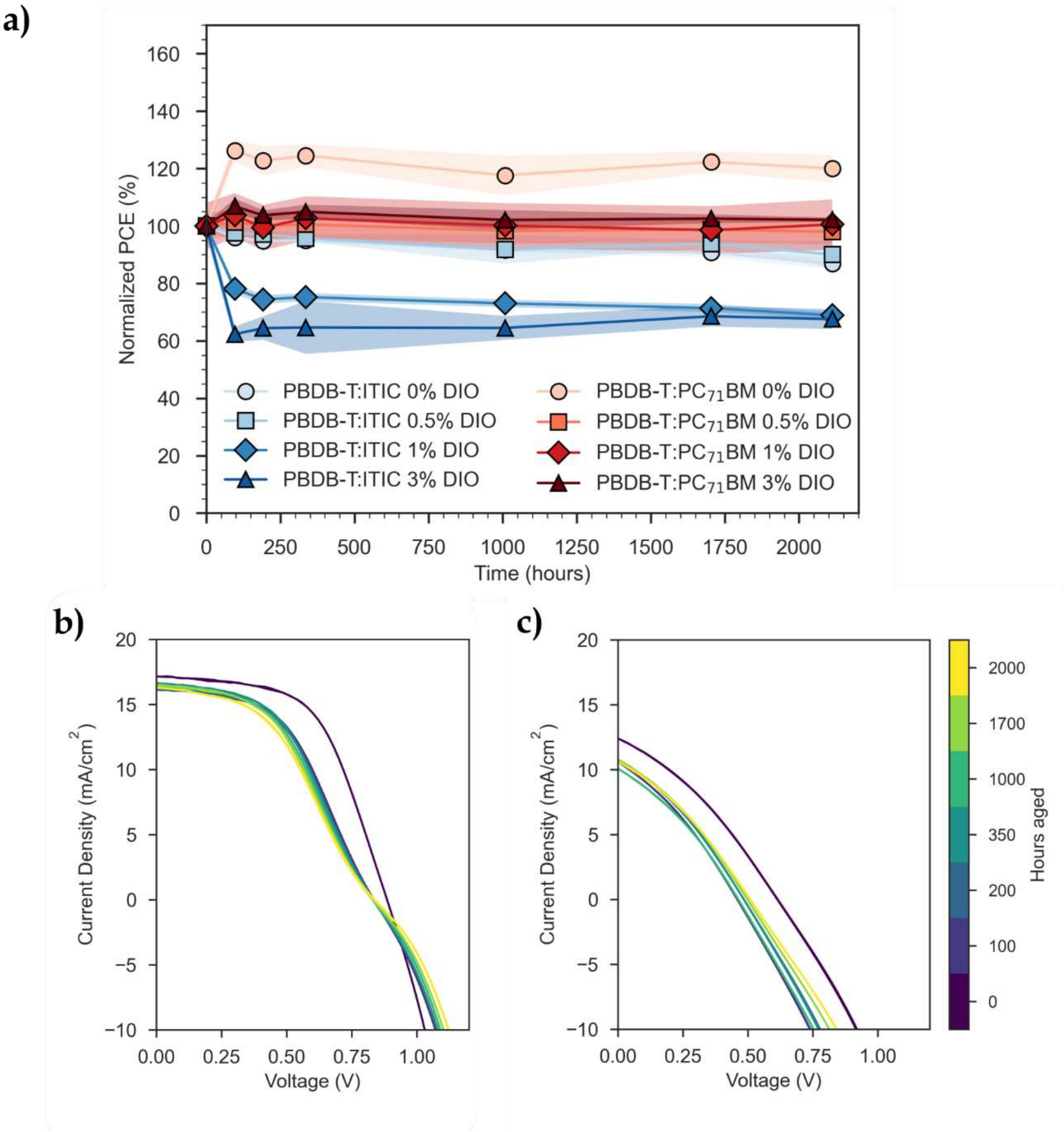

***Figure 3: a)** Normalized PCE of devices stored under dark conditions and in an inert atmosphere. Points given as an average of 3 devices, with the error bars representing ± 1 standard deviation. Corresponding evolution of the champion device for PBDB-T:ITIC based systems containing **b)** 1% and **c)** 3% DIO.*

The stability of all the devices based on PBDB-T:$PC_{71}BM$ is excellent, with some devices even showing a slight 'positive burn-in' in terms of performance, which has elsewhere been attributed to positive morphological changes.[10] With no, or only 0.5%, addition of DIO, the PBDB-T:ITIC based devices also show good morphological stability. In all these cases it can be considered that deleterious phase separation or chemical reactions are not occurring within the cell on these timescales (i.e. they are stable).

Upon addition of higher amounts of DIO, 1% and 3%, PBDB-T:ITIC based devices show a negative burn-in, dropping to below 80% of their initial performance within only a few days of ageing. In **Figure 3b** it can be seen clearly that the 's-shaped' *JV* curves are apparent in fresh 3% DIO devices, and begin to emerge in those using 1% DIO after time. This implies there is a gradual process influencing these characteristics, and that it is exacerbated by higher volumes of DIO. Whilst the process that induces the s-shaped curves may be specific to ITIC based devices, it also noteworthy that other studies[45] have seen higher volumes of DIO 'trapped' in PBDB-T:ITIC based systems compared to those using PBDB-T:$PC_{71}BM$, so this, and other processes linked to acceptor chemistry, may also be playing a role.

2.3 Exciton Diffusion Length

To further understand baseline differences in the charge carrier transport between the acceptors, the exciton diffusion length was studied for PBDB-T and ITIC. This has previously been established for $PC_{71}BM$ to be in the region of 3-5 nm.[46-48]

Exciton diffusion length can be measured via several different methods including external quantum efficiency (EQE) measurements, fluorescence quenching, and exciton-exciton annihilation.[49–52] Here, spectrally-resolved photoluminescence quenching is used to probe the exciton diffusion length.[53] This method involves measuring the photoluminescence excitation spectrum of the thin film of interest with and without an adjacent quenching layer. The ratio of this spectra is fit an optical transfer matrix model for the exciton diffusion length. Unlike thickness-dependent photoluminescence quenching, where the initial exciton profile is varied via active layer thickness, this method uses different pump wavelengths to realize the same outcome. Using this method, the results of which can be seen in **Figure S5 – S6**, exciton diffusion lengths of PBDB-T and ITIC were measured as 11.6 ± 0.60 nm and 12.7 ± 0.35 nm respectively. It is noted that the value for PBDB-T compares well to that found for similar structures in other studies,[54] however the value for ITIC is much lower than that of ~20 nm measured previously.[55,56]

We then sought to understand how these exciton diffusion lengths relate to other length scales within the BHJ, especially in the context of vertical segregation, and how this is influenced by both acceptor identity and the level of added DIO.

2.4 Characterizing Vertical Segregation of BHJ Films

To understand the impact of processing on the vertical chemical composition of the blend films, we performed contact angle goniometry and neutron reflectometry (NR) measurements. We first sought to estimate the surface energy of each blend component by measuring the contact angles of water and hexadecane droplets on the surface of neat ITIC, $PC_{71}BM$ and PBDB-T films (**Figure S7**). Using the Fowkes surface energy model (further details are provided in **Supplementary Note 2: Surface Energy Estimations**), surface energies were estimated to be 27.7 mN/m, 28.1 mN/m and 27.0 mN/m for ITIC, $PC_{71}BM$ and PBDB-T respectively (**Table S2**). The lower surface energy of PBDB-T compared to ITIC and $PC_{71}BM$ suggests that it is more energetically favorable for PBDB-T to segregate to the air interface in the blend films. Extending our contact angle study to blend films processed with different concentrations of DIO, we find that the total surface energy of both blend systems decreases when processing with higher concentrations of DIO, indicating an increase in vertical segregation between blend components (**Table S3**, **Figure S10**). This is in good agreement with results reported elsewhere,[57,58] and may be linked to the extended drying times facilitated by solutions having higher DIO content.

To explore whether the changes in surface energy correlate to changes in vertical segregation, the chemical composition of the blend films in the plane perpendicular to the substrate was characterized using NR. In an NR experiment, a beam of neutrons is directed at the surface of a film at a shallow angle, and the intensity of the neutrons reflected at various angles (and/or neutron wavelengths) is measured as a function of momentum transfer (often denoted as q). The resulting reflectometry curve is the fraction of neutrons reflected (R) versus q. To overcome the low SLD contrast in PBDB-T:ITIC blend films, we synthesized a deuterated ITIC analogue (ITIC-d_8) (full synthesis details and NMR characterization is provided in **Supplementary Note 3: ITIC-d_8 Synthesis and Characterization**).

NR data and associated fits for PBDB-T:ITIC-d_8 and PBDB-T:$PC_{71}BM$ blend films processed with 0-3% DIO concentration and deposited onto PEDOT:PSS coated silicon substrates are presented in **Figure 4a,b**. To assist in the data modelling, the NR of neat PEDOT:PSS, PBDB-T, ITIC-d_8 and $PC_{71}BM$ films were also measured to provide reference SLD values for each material (**Table S4**, **Figure S15**). In **Figure 4c,d**, the SLD profiles corresponding to the modelled NR data are plotted as a function of OPV blend thickness. All NR curves for the blend films were modelled as a stack of Si/SiO_2/PEDOT:PSS/OPV blend/Air where each layer in the sample represents a slab characterized by a thickness, roughness and SLD (fit parameters are displayed in **Table 2**). To further quantify vertical segregation in the blend films, thickness-dependent SLD profiles have been converted to an acceptor concentration by volume (ϕ_A) (**Figure 4e,f)**. Here, the SLD is assumed to be the volume weighted average of the acceptor (A) and donor (D) phases ($\phi_A + \phi_D = 1$):

$$SLD = \phi_A SLD_A + \phi_D SLD_D \quad (1)$$

$$\phi_A = \frac{SLD - SLD_D}{SLD_A - SLD_D} \quad (2)$$

For PBDB-T:ITIC-d_8 blend films, a single homogenous layer could not be successfully used to model the NR data, and it was necessary to add an ITIC-d_8-rich layer at the bottom film/PEDOT:PSS interface (**Figure 4a**). During fitting, the SLD of the buried interface layer progressed to the upper bound for all PBDB-T:ITIC-d_8 samples. To ensure fits remained physical, the SLD of the buried interface layer was fixed to the SLD of pure ITIC-d_8 (2.15×10^{-6}Å^{-2}) with changes in this interface modulated by the thickness and roughness of the layer. PBDB-T:ITIC-d_8 blends films processed with 0% and 0.5% DIO comprise a pure ITIC-d_8 buried interface layer and a mixed bulk layer with a composition of 53:47 PBDB-T:ITIC-d_8 by volume – a composition close to the mass ratio of the materials in solution (1:1). The relative thickness of the ITIC-d_8 interface layer compared to the total film thickness increases from 7% to 7.5% for 0 and 0.5% DIO respectively. In comparison, PBDB-T:ITIC-d_8 blend films processed with 1% DIO are characterized by a broadened ITIC-d_8 interface (11.1% relative thickness) and a change in composition of the bulk layer to 59:41 PBDB-T:ITIC-d_8 indicating increased vertical segregation between the blend components.

This effect is further emphasized in blends processed with 3% DIO, which are composed of an ITIC-d_8 interface with a relative film thickness of 11.8% and a bulk layer composition of 93:07 PBDB-T:ITIC. This dramatic change in bulk layer composition is ascribed to the combination of enhanced vertical segregation and the presence of higher quantities of residual DIO in the film as demonstrated in previous studies.[45] Large amounts of residual DIO in the film will reduce the average SLD of the blend significantly ($SLD_{DIO}= 0.118 \times 10^{-6}$ Å^{-2}),[14] and make it difficult to accurately determine composition as the blend comprises a mixture of three components (PBDB-T, ITIC-d_8 and DIO).

Similarly to ITIC-d_8 blend films, a single homogenous layer was insufficient to accurately model the NR data of PBDB-T:PC$_{71}$BM films, resulting in large chi-squared values (**Table S5**). To determine an appropriate model for data fitting, PBDB-T:PC$_{71}$BM blend films were modelled in three different ways; as a single homogenous bulk layer, as a bulk layer with an acceptor-rich buried interface and as a bulk layer with an acceptor-rich surface (**Figure S16**, **Table S5**). It is noted that the accumulation of acceptor would have different impacts on device performance depending on if the interface was with the hole or electron transporting layer (the latter being favorable for electron transport, and the former being unfavorable).

Fits with an acceptor-rich surface generally resulted in an interface roughness that was comparable to the thickness of the interface. Additionally, given that surface energy estimates indicate that a PBDB-T-rich surface is more energetically favorable, a bulk layer with an acceptor-rich buried layer was selected as the most physical model (**Figure 4b**). Consequently, all PBDB-T:$PC_{71}BM$ blend films in this study comprise a bulk layer with a $PC_{71}BM$ volume concentration in the range 38% - 45%, and an acceptor-rich layer at the film/PEDOT:PSS interface with a relative thickness that is comparable across all samples (~14% - 16% of the total blend film thickness). Processing with DIO results in an increase in the segregation of $PC_{71}BM$ to the buried interface, from ~47% without DIO to ~60%, ~63% and ~67% for films processed with 0.5, 1 and 3% DIO, respectively.

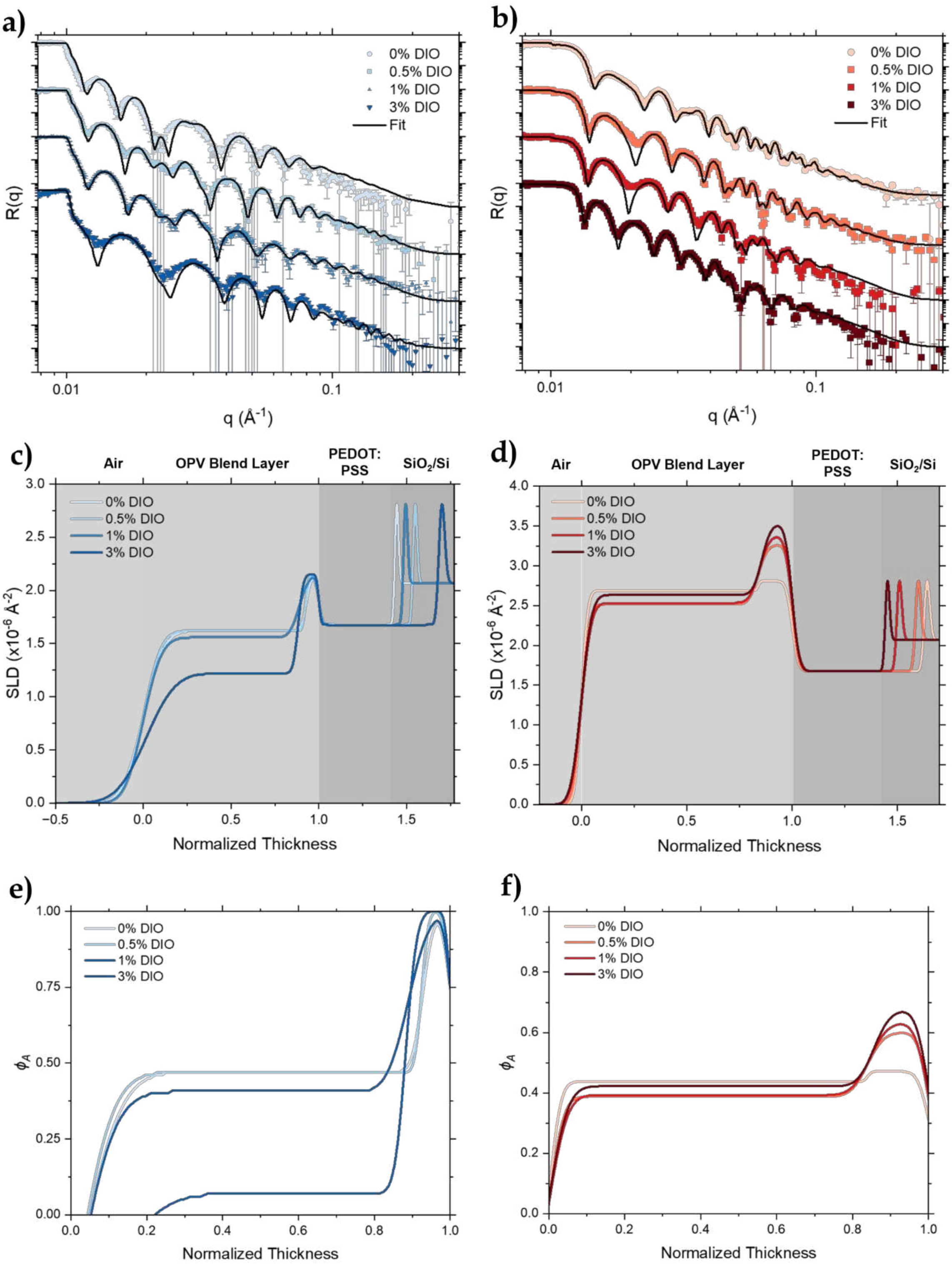

Figure 4: *Neutron reflectometry data for of* ***a)*** *PBDB-T:ITIC-d$_8$ and* ***b)*** *PBDB-T:PC$_{71}$BM blend films processed with 0-3% added DIO on PEDOT:PSS coated silicon substrates with associated fits (black line). The reflectivity (R(q)) data has been offset by two decades for clarity. Corresponding SLD profiles for* ***c)*** *PBDB-T:ITIC-d$_8$ and* ***d)*** *PBDB-T:PC$_{71}$BM blend thin films (SLDs for each blend component are as follows: SLD$_{PBDB\text{-}T}$ = 1.15 ×10^{-6}Å^{-2}, SLD$_{ITIC\text{-}d8}$ = 2.15 ×10^{-6}Å^{-2} and SLD$_{PC71BM}$ = 4.67 ×10^{-6}Å^{-2}). Thickness has been normalized to the thickness of the OPV blend film where 0 is the midpoint of the air/film interface and 1 is the midpoint of the film/PEDOT:PSS interface. Acceptor concentration by volume (ϕ_A) as a function of film depth calculated from the SLD profiles using Equation (2) for* ***e)*** *PBDB-T:ITIC-d$_8$ and* ***f)*** *PBDB-T:PC$_{71}$BM blend films.*

Table 2: *Key NR model parameters for the data fits shown in Figure 4. The full model fitting parameters are provided in Table S5 and Table S6. Relative thicknesses are the percentage thickness of the interface layer compared to the total thickness of the blend film.*

Blend System	DIO Concentration (Vol%)	Bulk Layer				Interface Layer				χ^2/N_{pts}
		Thickness (Å)	Roughness (Å)	SLD ($\times10^{-6}$Å^{-2})	Relative Thickness (%)	Thickness (Å)	Roughness (Å)	SLD ($\times10^{-6}$Å^{-2})	Relative Thickness (%)	
PBDB-T:ITIC-d$_8$	0	798	79	1.62	93.0	60	19	2.15	7.0	2.88
	0.5	723	62	1.62	92.5	59	11	2.15	7.5	3.73
	1	692	64	1.56	88.9	86	34	2.15	11.1	2.19
	3	462	70	1.22	88.2	62	12	2.15	11.8	6.15
PBDB-T:PC$_{71}$BM	0	566	16	2.69	83.9	109	5	2.81	16.1	5.04
	0.5	597	21	2.52	83.8	115	24	3.26	16.2	17.50
	1	635	29	2.53	84.4	117	28	3.38	15.6	16.68
	3	754	35	2.64	85.6	127	29	3.52	14.4	6.20

These results suggest that processing with DIO results in enhanced vertical segregation in both ITIC and PC$_{71}$BM based systems, however the segregation appears to be substantially more pronounced in PBDB-T:ITIC systems resulting in a pure acceptor buried interface layer as visualized in **Figure 5**. Given the similarity in Flory–Huggins interaction parameters estimated for PBDB-T with ITIC and PC$_{71}$BM,[57] and their similar solubilities in DIO,[59] we suspect this effect is primarily driven by differences in the film drying dynamics, kinetic hindrance, or higher levels of residual DIO in PBDB-T:ITIC based systems.[45]

The thickness of this buried interface layer increases with increasing DIO concentrations. Whilst segregation also occurs for PBDB-T:PC$_{71}$BM based systems, no pure acceptor layer is formed, and the components at the HTL interface remain mixed.

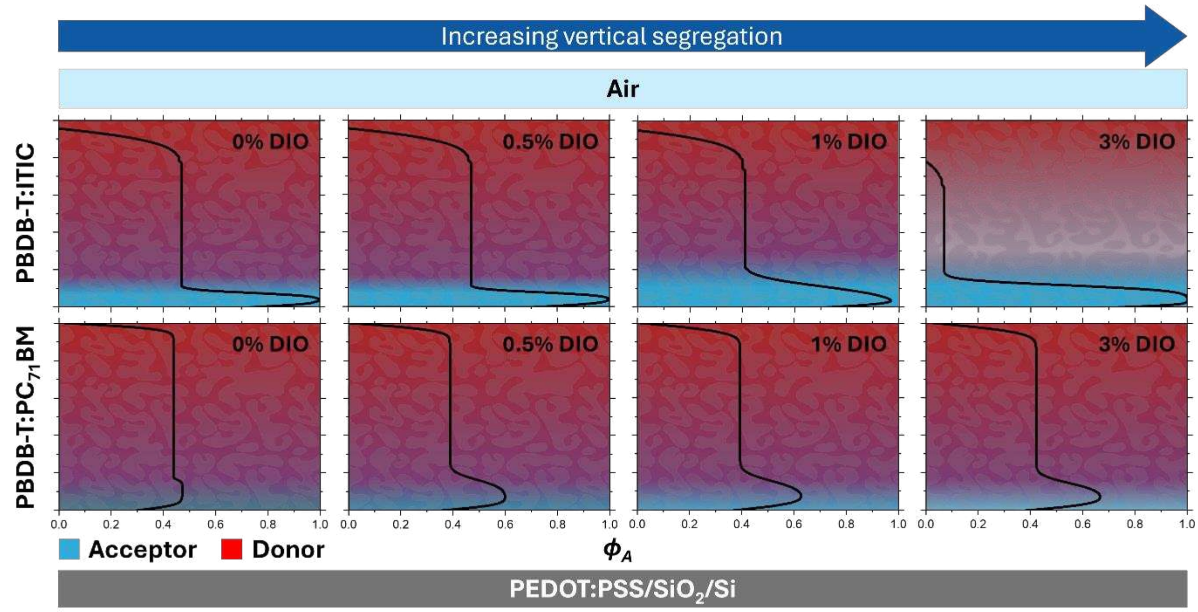

***Figure 5**: Illustration of the impact of DIO processing on vertical segregation in PBDB-T:ITIC and PBDB-T:PC$_{71}$BM blend films. Overlayed are the acceptor volume concentration (ϕ_A) profiles extracted from NR measurements (Figure 4), illustrating the pure ITIC interface, but mixed PBDB-T:PC$_{71}$BM interface.*

2.5 J-V Curve Simulations

To better understand how an interface composed of pure acceptor at the HTL might impact the solar cell device *JV* characteristics, simulations were carried out using OghmaNano, a drift-diffusion based model that includes carrier trap states.[60–63] Here an interface of pure ITIC was simulated between the PEDOT:PSS HTL and the BHJ (shown in **Figure 6a**). The thickness chosen for the interface layer matched the relative thickness measured using NR (**Table 2**). It is important to note that at the highest DIO concentrations, the pure interface layer of ITIC approaches the exciton diffusion length determined in **Section 2.3**, however the greatest impact is anticipated to be on the transport and collection of dissociated holes, rather than excitons, due to the unfavorable energy level alignment between ITIC and PEDOT:PSS (**Figure 6b**).

The model was fit to *JV* curves from devices aged for 1 week, matching the time period of the NR measurements, by following procedures published elsewhere,[64] and further outlined in the **Experimental Methods.** PBDB-T:PC$_{71}$BM blend devices were not simulated due to the mixed nature of the PC$_{71}$BM interfacial layer. Electrical parameters were allowed to vary between devices with different DIO concentrations, as would be expected by the effect of the significant morphological changes mediated by DIO.[34,45]

The resulting fits can be seen in **Figure 6c-f**. This demonstrates that the experimentally observed differences in the *JV* curve behavior, as a result of different DIO concentrations, can be attributed to changes in the interface layer. Although charge carrier mobility was important, the parameter which differed the most between DIO concentrations was the free-to-free recombination cross section (see model parameters in **Table S7**). Thus, we suspect the blocking layer is not only introducing an energetic barrier, but also acting as a recombination center, due to its non-optimal phase segregation. Charge build-up is also confirmed by the increases in trapped carrier density at the buried interface (**Figure S17**). These results strongly suggest that the pure ITIC build-up measured in the NR is the primary cause of the observed s-shaped *JV* curve behavior.

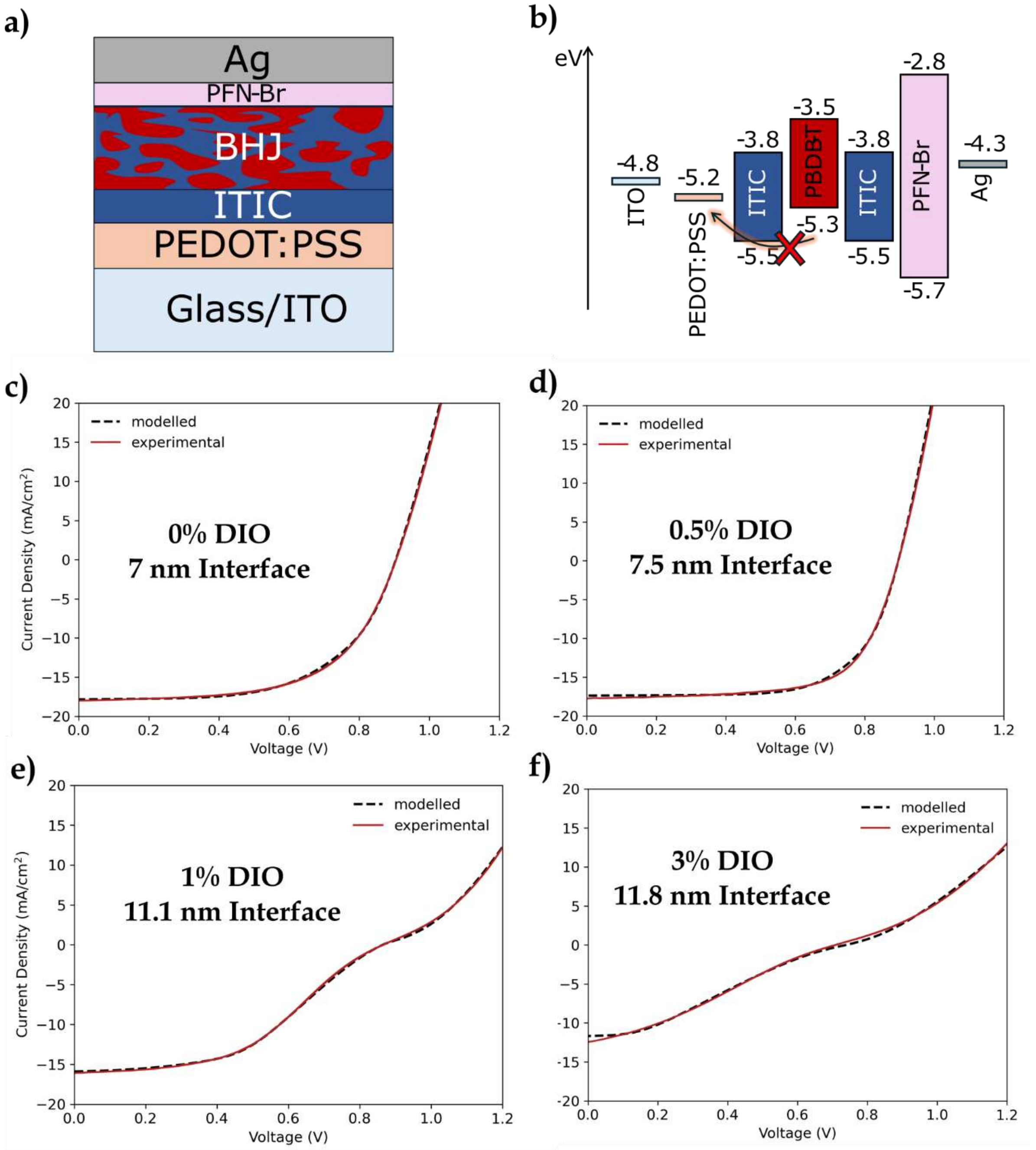

Figure 6: ***a)*** *Simulated stack, with pure ITIC interface between bulk and PEDOT:PSS,* ***b)*** *approximate energy levels, showing the barrier for hole transport to the PEDOT:PSS (values taken from literature).*[65,66] *Modelled and experimental JV curves for devices based on PBDB-T:ITIC with* ***c)*** *0% DIO,* ***d)*** *0.5% DIO,* ***e)*** *1% DIO and* ***f)*** *3% DIO. The thickness of the interfacial layer was set to values determined from the neutron reflectivity measurements (Table 2).*

These simulations were then used to understand the mechanisms at work in experimental devices. With high amounts of DIO (3%), s-shaped curves are seen in fresh devices, suggesting the initial vertical segregation (potentially combined with other DIO mediated morphological effects), is severe enough to result in a buried ITIC interface, and corresponding effects described above. With lower amounts (1%), s-shaped curves only emerge after a few days (**Figure 3b**), implying segregation is also a gradual process; likely aided by residual DIO plasticizing the BHJ.

With very low amounts of DIO (0, 0.5%) and with a different acceptor ($PC_{71}BM$), s-shaped curves are not observed in fresh or aged devices. In the former case, we believe the segregation is small enough to prevent overly significant charge build-up, a suggestion supported by the significantly lower simulated recombination rate in the interface layer for these concentrations compared to those higher (**Table S7**). In the latter case, the NR shows that the interface formed is not pure, implying hole transport can still take place to allow more ideal device function.

These proposed mechanisms are reflected in **Figure 3a**, where we see good morphological stability for PBDB-T:ITIC devices with 0 or 0.5% DIO, but significant burn in for those using 1 or 3% DIO. It is likely here that high amounts initial of DIO lead to more significant component diffusion as a result of residual additive, and so more significant vertical segregation over time, yielding reduced device performance due to charge build-up.

3. Conclusions

This work has explored the relationship between film processing, vertical segregation, device performance and stability in both PBDB-T:ITIC and PBDB-T:$PC_{71}BM$ OPV blend systems. Whilst PBDB-T:$PC_{71}BM$ devices demonstrate ideal *JV* behavior, PBDB-T:ITIC devices fabricated from high concentrations of DIO (3%) resulted in non-ideal ‘s-shaped’ *JV* curves. This has previously been attributed to the formation of a charge injection or a charge extraction barrier. During device ageing measurements, we find that s-shaped curves also emerge in PBDB-T:ITIC devices processed with lower concentrations of DIO (1%), implying the production of such barriers is a dynamic process with implications for device stability.

Using NR, we are able to correlate vertical segregation effects to device *JV* measurements, showing that both systems demonstrate vertical segregation with an enrichment of the acceptor material at the film/HTL interface. However, the severity of such segregation is much greater for ITIC-based systems compared to $PC_{71}BM$-based systems with films composed of a near pure enriched ITIC layer at the HTL interface. Processing with the solvent additive DIO results in increased vertical segregation, characterized by a broadening of the pure acceptor layer in ITIC-based systems and an enrichment of the acceptor at the HTL interface in $PC_{71}BM$-based systems. Vertical segregation in both systems is likely driven by the extended drying times facilitated by the high boiling point of DIO allowing for greater segregation, due to the energetic favorability of the low surface energy component at the air interface. However, we note segregation, and the differences between the two blend systems, may also be influenced by other factors such as molecular structure and differences in the amount of residual DIO retained in films after processing.[45] Through drift-diffusion simulations we show that the severe vertical segregation measured by NR is directly related to the s-shaped *JV* curves observed in PBDB-T:ITIC devices, due to the pure ITIC layer inducing a charge build-up at the PEDOT:PSS interface.

We note that alongside the DIO induced vertical segregation, there may be other interactions between DIO and the OPV components at play, including reactions, that could induce s-shaped *JV* curves. Here we discount damaging chemical reactions between DIO and PEDOT:PSS due to the stability of the V_{OC} in aged PBDB-T:ITIC devices with 1% DIO (**Figure S1c**); and similar processes between DIO and the active layer due to the retention and stability of a high J_{SC} (**Figure S1b**). Deleterious morphological changes, such as aggregation, that are exacerbated by DIO may be contributing to poor charge transport characteristics.

It is likely that the conclusions in this work are broadly applicable to other NFA systems, and those using other high boiling point solvent additives. In general, prolonged drying times will exacerbate vertical segregation and crystallization, with the caveat that other factors such as relative component solubility and additive retention rates may also play a role. It is clear that solvent additives can be a method of vertical segregation control, but also that this must be done carefully, as high amounts of solvent additive can yield severe interfacial stratification, and instability. The use of more volatile additives, solid additives or designing OPV architectures around likely donor-acceptor segregation patterns (for example using an inverted architecture), are possible strategies to prevent these problems, although it is noted that in general high rates of component diffusion will be unfavorable regardless of architecture. In the move towards larger area fabrication, this work illustrates that regulation of solvent evaporation is important to control vertical morphology in other deposition techniques, for example use of a heated stage in blade coating to overcome the intrinsically longer drying times.

4. Experimental Methods

Materials

All solvents were purchased from Sigma Aldrich. PBDB-T (M_w: 90,311 g/mol) ITIC and $PC_{71}BM$ (99% purity) were purchased from Ossila. Solid materials were stored in the glovebox but weighed out in air, with solvents added inside a glovebox with a nitrogen atmosphere.

Organic Solar Cell Fabrication

Devices were manufactured on 8-pixel, pre-patterned ITO substrates (Ossila, batch S211). Substrates were cleaned by step-wise sonication in dilute Hellmanex III (Ossila), deionized water and isopropyl alcohol, with each step lasting 10 minutes in a water bath held at ~50 °C. Following cleaning the substrates were dried with a N_2 gun and exposed to UV-ozone for 15 minutes. PEDOT:PSS (Ossila, Al 4083) was filtered through a 0.45 μm PVDF microdisc filter before use. A ~30 nm PEDOT:PSS layer was coated via dynamic spin coating in air at 6000 rpm for 30 seconds. The ITO was exposed via patterning using a cotton bud dipped in water. The films were then annealed at 110°C for 15 minutes in air and transferred to a N_2 filled glovebox, followed by a further anneal at 110 °C for 15 minutes. Active layer solutions were made at either 15 mg/mL (PBDB-T:$PC_{71}BM$) or 18 mg/mL (PBDB-T:ITIC), at a weight ratio of 1:1 in chlorobenzene and stirred overnight at 60 °C before use. The relevant amount of DIO for each solution was added at the same time as the chlorobenzene, usually from a stock solution. PBDB-T:$PC_{71}BM$ films were spin coated dynamically at 1000 rpm for 40 seconds, PBDB-T:ITIC films were spin coated dynamically at 2000 rpm for 40 seconds, both to achieve a film thickness of ~100 nm. All films were annealed at 160 °C for 10 minutes. PFN-Br (Ossila, M_w: 165,000 g/mol) solutions were made at 0.5 mg/mL in methanol and stirred overnight without heating before use. PFN-Br films were spin coated dynamically in a glovebox at 3000 rpm for 30 seconds without anneal. The ITO was exposed by scraping the films off using a razor blade. An Ag cathode (100 nm) was then thermally evaporated at a pressure of 2×10^{-6} mbar through a shadow mask with a defined pixel area of 4 mm^2.

Following electrode deposition, devices were encapsulated using a UV curable epoxy (Ossila), which was dropped onto the substrate, topped with a glass slide, and cured for 15 minutes under a lamp at ~365 nm. All layer thicknesses were measured using a Bruker DetakXT profilometer. *JV* sweeps were measured using a Newport 92251A-1000 solar simulator which had been calibrated using a certified silicon reference cell. Devices were illuminated through an aperture mask with each pixel area restricted to 0.0256 cm^2.

For characterization measurements, blend films were prepared following the same device film protocols outlined above. Neat ITIC, $PC_{71}BM$ and PBDB-T films were prepared at a solid concentration of 15 mg/mL in chlorobenzene using the same DIO concentrations and annealing procedures as for blend films.

Organic Solar Cell Stability Testing

Aged devices were kept in a N_2 filled glovebox maintained at ~23°C and >0.1ppm H_2O & O_2 and removed to air for periodic testing.

Exciton Diffusion Length Measurements

Exciton diffusion measurements of PBDB-T and ITIC involved fabricating a series of exciton-quenched and exciton-unquenched samples composed of PBDB-T and ITIC films deposited onto an electron-blocking layer (HfO_2) with different capping layers. The exciton diffusion length was then measured using spectrally resolved PL quenching following previous protocols.[53] Full sample preparation and measurement details are provided in Supplementary Note 1: Exciton Diffusion Length Measurements.

Contact Angle Measurements

Contact angle measurements were carried out using an Ossila goniometer. The contact angle of water and hexadecane droplets on film surfaces were recorded and analyzed using the Ossila Contact Angle software. A baseline was fitted to the droplet/substrate interface and adjusted for any sample or camera tilt. Contact angle values are the average of the two angles (left and right) measured for each droplet. Surface energy estimations were made using the Fowkes model (further details provided in SI).

Neutron Reflectometry

Neutron reflectivity measurements were performed using the D17 reflectometer at Institut-Laue-Langevin (ILL), Grenoble, France.[67]All samples were made fresh and stored in nitrogen sealed bags before transit to D17 at ILL for measurement ~1 week later. Blend films were spin-coated onto PEDOT:PSS coated silicon substrates (5cm diameter) following the same protocols used for device fabrication. Pure material reference films were spin-coated directly onto clean silicon substrates. D17 is a horizontal geometry (vertical surfaces) neutron reflectometer, which operates in time-of-flight (TOF) mode. In this configuration, neutrons with a broad range of wavelengths (2 to 27Å) are incident on the sample and reflected neutrons are detected using an area detector. This allows both off-specular and specular scattering to be rapidly probed across a large q range. The reflectometry measurements in this work were collected using incident angles of 1° and 4°, generating a q range of 0.0076 - 0.317 $Å^{-1}$. Neutrons were counted for 30 min and 100 min at the lower and higher angles, respectively, and collimation was chosen such that samples were under-illuminated. Specular neutron reflectivity curves were extracted from the raw incident and reflected neutron beams using the COSMOS data reduction program.[68] Data was fitted using GenX software using an instrumental resolution of 2%.[69]

JV Curve Simulations

OghmaNano was used for all *JV* simulations. The software's in-built material files were used for the glass, ITO, silver, PEDOT:PSS and PBDB-T:ITIC layers. As PFN-Br was not an in-built material, ZnO was used in its place, due to their similar function and energy levels. All layer thicknesses were kept consistent with experimental values from the NR measurements and device preparation, with an absolute active layer thickness of 100nm used (including the pure ITIC interface).

The in-built Shockley-read-hall carrier trapping and recombination functions were used, with model parameters given in **Table S7**. Blend mobility values[70] and HOMO and LUMO levels[65] were initially set to those from literature, before experimental *JV* sweeps were fitted using OghmaNano's inbuilt fitting function. The charge carrier mobilities, recombination rates, HOMO and LUMO levels and relative permittivity for the BHJ and interfacial layer, shunt resistance, series resistance and photon efficiency for the device were used as fitting parameters for the 3% concentration of DIO. The LUMO levels and relative permittivities were then fixed, with the remaining parameters allowed to float to fit the remaining DIO concentrations.

Supporting Information

The supporting information file includes additional data and information concerning organic solar cell devices and stability, contact angle measurements, surface energy estimations, ITIC-d_8 synthesis and characterization, neutron reflectometry, exciton diffusion length measurements and additional JV simulation details.

Data Availability

NR data is stored in the ILL data repository (doi:10.5291/ILL-DATA.9-11-1957).

Author Contribution Statement (if required)

E.L.K.S and R.C.K designed the experiments and prepared samples for characterization. E.L.K.S performed device fabrication, testing and stability measurements, and JV simulations. R.C.K analyzed the NR data and performed contact angle measurements and related analysis. J.C and T.W synthesized the deuterated ITIC analogue and performed NMR characterization. K.S and R.J.H performed exciton diffusion length measurements and analysis. R.M. created OghmaNano software and assisted with drift-diffusion simulations. E.J.C assisted with stability measurements, data analysis and editing. P.G. performed NR measurements. A.J.P, D.G.L and R.A.L.J supervised the study. All authors contributed to writing the manuscript.

Conflict of Interest

D.G.L. is a co-director of the company Ossila Ltd (www.ossila.com) which retails materials and equipment used in organic photovoltaic device research and development.

Acknowledgements

The authors acknowledge funding through the Engineering and Physical Sciences Research Council (EPSRC) via grants EP/V055127/1, EP/V027131/1 and EP/Y031962/1. E.L.K.S thanks the EPSRC for a PhD studentship from the Centre for Doctoral Training in New and Sustainable PV (EP/L01551X/10) and Innovate UK for postdoctoral funding under project number 10030528. R.C.K thanks the University of Sheffield for funding through a departmental teaching PhD scholarship and the award of a publication scholarship. The authors are grateful to Institut Laue-Langevin (ILL) for the award of beamtime on the D17 reflectometer under experimental number 9-11-1957. R.J.H. acknowledges support from Ronald L. and Janet A. Christenson, a Leverhulme Trust Visiting Professorship at the University of Cambridge and a Visiting Fellowship at Clare Hall, University of Cambridge. K.S. acknowledges support from a University of Minnesota Doctoral Dissertation Fellowship.

References

(1) Riede, M.; Spoltore, D.; Leo, K. Organic Solar Cells—The Path to Commercial Success. *Adv. Energy Mater.* **2021**, *11* (1), 2002653. DOI: 10.1002/aenm.202002653.

(2) Li, Y.; Huang, X.; Sheriff Jr, H. K. M.; Forrest, S. R. Semitransparent organic photovoltaics for building-integrated photovoltaic applications. *Nat. Rev. Mat.* **2023**, *8*, 186-201. DOI: 10.1038/s41578-022-00514-0.

(3) Suthar, R.; Dahiya, H.; Karak, S.; Sharma, G. D. Indoor Organic Solar Cells for Low-Power IoT Devices: Recent Progress, Challenges, and Applications. *J. Mater. Chem. C* **2023**, *11* (37), 12486–12510. DOI: 10.1039/D3TC02570E.

(4) Guan, S.; Li, Y.; Xu, C.; Yin, N.; Xu, C.; Wang, C.; Wang, M.; Xu, Y.; Chen, Q.; Wang, D.; Zuo, L.; Chen, H. Self-Assembled Interlayer Enables High-Performance Organic Photovoltaics with Power Conversion Efficiency Exceeding 20%. *Adv. Mater.* **2024**, *36* (25), 2400342. DOI: 10.1002/adma.202400342.

(5) Chen, C.; Wang, L.; Xia, W.; Qiu, K.; Guo, C.; Gan, Z.; Zhou, J.; Sun, Y.; Liu, D.; Li, W.; Wang, T. Molecular Interaction Induced Dual Fibrils towards Organic Solar Cells with Certified Efficiency over 20%. *Nat. Commun.* **2024**, *15* (1), 6865. DOI: 10.1038/s41467-024-51359-w.

(6) Ding, P.; Yang, D.; Yang, S.; Ge, Z. Stability of Organic Solar Cells: Toward Commercial Applications. *Chem. Soc. Rev.* **2024**, *53* (5), 2350–2387. DOI: 10.1039/D3CS00492A.

(7) Lee, H.; Park, C.; Sin, D. H.; Park, J. H.; Cho, K. Recent Advances in Morphology Optimization for Organic Photovoltaics. *Adv. Mater.* **2018**, *30* (34), 1800453. DOI: 10.1002/adma.201800453.

(8) Huang, L.; Wang, G.; Zhou, W.; Fu, B.; Cheng, X.; Zhang, L.; Yuan, Z.; Xiong, S.; Xhang, L.; Xie, Y.; Xhang, A.; Zhang, Y.; Ma, W.; Li, W.; Zhou, Y.; Reichmanis, E.; Chen, Y. Vertical Stratification Engineering for Organic Bulk-Heterojunction Devices. *ACS Nano* **2018**, *12* (5), 4440-4452. DOI: 10.1021/acsnano.8b00439.

(9) Yan, Y.; Liu, X.; Wang, T. Conjugated-Polymer Blends for Organic Photovoltaics: Rational Control of Vertical Stratification for High Performance. *Adv. Mater.* **2017**, *29* (20), 1601674. DOI: 10.1002/adma.201601674.

(10) Ghasemi, M.; Hu, H.; Peng, Z.; Rech, J. J.; Angunawela, I.; Carpenter, J. H.; Stuard, S. J.; Wadsworth, A.; McCulloch, I.; You, W.; Ade, H. Delineation of Thermodynamic and Kinetic Factors that Control

Stability in Non-fullerene Organic Solar Cells. *Joule* **2019**, *3* (5), 1328-1348. DOI: 10.1016/j.joule.2019.03.020.

(11) Li, X.; Zhu, R.; He, Z.; Du, X.; Lin, H.; Zheng, C.; Yang, G.; Chen, Z.; Tao, S. Additive-Induced Vertical Component Distribution Enables High-Performance Sequentially Cast Organic Solar Cells. *ACS Appl. Mater. Interfaces* **2022**, *14* (22), 25842–25850. DOI: 10.1021/acsami.2c04997.

(12) Karagiannidis, P. G.; Georgiou, D.; Pitsalidis, C.; Laskarakis, A.; Logothetidis, S. Evolution of vertical phase separation in P3HT:PCBM thin films induced by thermal annealing. *Mater. Chem. Phys.* **2011**, *129* (3), 1207-1213. DOI: 10.1016/j.matchemphys.2011.06.007.

(13) Kovalenko, A.; Stoyanova, D.; Pospisil, J.; Zhivkov, I.; Fekete, L.; Karashanova, D.; Kratochvílová, I.; Vala, M.; Weiter, M. Morphology versus Vertical Phase Segregation in Solvent Annealed Small Molecule Bulk Heterojunction Organic Solar Cells. *Int. J. Photoenergy* **2015**, *2015* (1), 238981. DOI: 10.1155/2015/238981.

(14) Zhang, Y.; Parnelll, A. J.; Pontecchiani, F.; Cooper, J. F. K.; Thompson, R. L.; Jones, R. A. L.; King, S. M.; Lidzey, D. G.; Bernardo, G. Understanding and controlling morphology evolution via DIO plasticization in PffBT4T-2OD/PC71BM devices. *Sci. Rep.* **2017**, *7*, 44269. DOI: 10.1038/srep44269.

(15) Love, J. A.; Chou, S.-H.; Huang, Y.; Bazan, G. C.; Nguyen, T.-Q. Effects of Solvent Additive on "s-Shaped" Curves in Solution-Processed Small Molecule Solar Cells. *Beilstein J. Org. Chem.* **2016**, *12* (1), 2543–2555. DOI: 10.3762/bjoc.12.249.

(16) Kim, M.; Kim, J.-H.; Choi, H. H.; Park, J. H.; Jo, S. B.; Sim, M.; Kim, J. S.; Jinnai, H.; Park, Y. D.; Cho, K. Electrical Performance of Organic Solar Cells with Additive-Assisted Vertical Phase Separation in the Photoactive Layer. *Adv. Energy Mater.* **2014**, *4* (2), 1300612. DOI: 10.1002/aenm.201300612.

(17) Li, Q.; Wang, L.-M.; Liu, S.; Zhan, X.; Zhu, T.; Cao, Z.; Lai, H.; Zhao, J.; Cai, Y.; Xie, W.; Huang, F. Impact of Donor–Acceptor Interaction and Solvent Additive on the Vertical Composition Distribution of Bulk Heterojunction Polymer Solar Cells. *ACS Appl. Mater. Interfaces* **2019**, *11* (49), 45979–45990. DOI: 10.1021/acsami.9b15753.

(18) Griffin, M. P.; Gearba, R.; Stevenson, K. J.; Vanden Bout, D. A.; Dolocan, A.Revealing the Chemistry and Morphology of Buried Donor/Acceptor Interfaces in Organic Photovoltaics. *J. Phys. Chem. Lett.* **2017**, *8* (13), 2764-2773. DOI: 10.1021/acs.jpclett.7b00911.

(19) Clark, M. D.; Jespersen, M. L.; Patel, R. J.; Leever, B. J. Predicting Vertical Phase Segregation in Polymer-Fullerene Bulk Heterojunction Solar Cells by Free Energy Analysis. *ACS Appl. Mater. Interfaces* **2013**, *5* (11), 4799–4807. DOI: 10.1021/am4003777.

(20) Germack, D. S.; Chan, C. K.; Kline, R. J.; Fischer, D. A.; Gundlach, D. J.; Toney, M. F.; Richter, L. J.; DeLongchamp, D. M. Interfacial Segregation in Polymer/Fullerene Blend Films for Photovoltaic Devices. *Macromolecules* **2010**, *43* (8), 3828–3836. DOI: 10.1021/ma100027b.

(21) Shin, N.; Kang, J.; Richter, L. J.; Prabhu, V. M.; Kline, R. J.; Fischer, D. A.; DeLongchamp, D. M.; Toney, M. F.; Satija, S. K.; Gundlach, D. J.; Purushothaman, B.; Anthony, J. E.; Yoon, D. Y. Vertically Segregated Structure and Properties of Small Molecule–Polymer Blend Semiconductors for Organic Thin-Film Transistors. *Adv. Funct. Mater.* **2013**, *23* (3), 366–376. DOI: 10.1002/adfm.201201389.

(22) Kirschner, S. B.; Smith, N. P.; Wepasnick, K. A.; Katz, H. E.; Kirby, B. J.; Borchers, J. A.; Reich, D. H. X-Ray and Neutron Reflectivity and Electronic Properties of PCBM-Poly(Bromo)Styrene Blends and Bilayers with Poly(3-Hexylthiophene). *J. Mater. Chem.* **2012**, *22* (10), 4364–4370. DOI: 10.1039/C2JM14967B.

(23) Yan, Y.; Liu, X.; Wang, T. Conjugated-Polymer Blends for Organic Photovoltaics: Rational Control of Vertical Stratification for High Performance. *Adv. Mater.* **2017**, *29* (20), 1601674. DOI: 10.1002/adma.201601674.

(24) Hynes, E. L.; Cabral, J. T.; Parnell, A. J.; Gutfreund, P.; Welbourn, R. J. L.; Dunbar, A. D. F.; Môn, D.; Higgins, A. M. Interfacial Width and Phase Equilibrium in Polymer-Fullerene Thin-Films. *Commun. Phys.* **2019**, *2* (1), 1–13. DOI: 10.1038/s42005-019-0211-z.

(25) Staniec, P. A.; Parnell, A. J.; Dunbar, A. D. F.; Yi, H.; Pearson, A. J.; Wang, T.; Hopkinson, P. E.; Kinane, C.; Dalgliesh, R. M.; Donald, A. M.; Ryan, A. J.; Iraqi, A.; Jones, R. A. L.; Lidzey, D. G. The Nanoscale Morphology of a PCDTBT:PCBM Photovoltaic Blend. *Adv. Energy Mater.* **2011**, *1* (4), 499–504. DOI: 10.1002/aenm.201100144.

(26) Wang, T.; Scarratt, N. W.; Yi, H.; Coleman, I. F.; Zhang, Y.; Grant, R. T.; Yao, J.; Skoda, M. W. A.; Dunbar, A. D. F.; Jones, R. A. L.; Iraqi, A.; Lidzey, D. G. Vertical Stratification and Its Impact on Device Performance in a Polycarbazole Based Copolymer Solar Cells. *J. Mater. Chem. C* **2015**, *3* (16), 4007–4015. DOI: 10.1039/C4TC02884H.

(27) Kingsley, J. W.; Marchisio, P. P.; Yi, H.; Iraqi, A.; Kinane, C. J.; Langridge, S.; Thompson, R. L.; Cadby, A. J.; Pearson, A. J.; Lidzey, D. G.; Jones, R. A. L.; Parnell, A. J. Molecular Weight Dependent Vertical

Composition Profiles of PCDTBT:PC71BM Blends for Organic Photovoltaics. *Sci. Rep.* **2014**, *4* (1), 5286. DOI: 10.1038/srep05286.

(28) Parnell, A. J.; Dunbar, A. D. F.; Pearson, A. J.; Staniec, P. A.; Dennison, A. J. C.; Hamamatsu, H.; Skoda, M. W. A.; Lidzey, D. G.; Jones, Richard. A. L. Depletion of PCBM at the Cathode Interface in P3HT/PCBM Thin Films as Quantified via Neutron Reflectivity Measurements. *Adv. Mater.* **2010**, *22* (22), 2444–2447. DOI: 10.1002/adma.200903971.

(29) Zhang, J.; Kan, B.; Pearson, A. J.; Parnell, A. J.; Cooper, J. F. K.; Liu, X.-K.; Conaghan, P. J.; Hopper, T. R.; Wu, Y.; Wan, X.; Gao, F.; Greenham, N. C.; Bakulin, A. A.; Chen, Y.; Friend, R. H. Efficient Non-Fullerene Organic Solar Cells Employing Sequentially Deposited Donor–Acceptor Layers. *J. Mater. Chem. A* **2018**, *6* (37), 18225–18233. DOI: 10.1039/C8TA06860G.

(30) Li, Q.; Wang, L.-M.; Liu, S.; Guo, L.; Dong, S.; Ma, G.; Cao, Z.; Zhan, X.; Gu, X.; Zhu, T.; Cai, Y.-P.; Huang, F. Vertical Composition Distribution and Crystallinity Regulations Enable High-Performance Polymer Solar Cells with >17% Efficiency. *ACS Energy Lett.* **2020**, *5* (11), 3637–3646. DOI: 10.1021/acsenergylett.0c01927.

(31) Wang, L.-M.; Li, Q.; Liu, S.; Cao, Z.; Cai, Y.-P.; Jiao, X.; Lai, H.; Xie, W.; Zhan, X.; Zhu, T. Quantitative Determination of the Vertical Segregation and Molecular Ordering of PBDB-T/ITIC Blend Films with Solvent Additives. *ACS Appl. Mater. Interfaces* **2020**, *12* (21), 24165–24173. DOI: 10.1021/acsami.0c02843.

(32) Kosco, J.; Bidwell, M.; Cha, H.; Martin, T.; Howells, C. T.; Sachs, M.; Anjum, D. H.; Gonzalez Lopez, S.; Zou, L.; Wadsworth, A.; Zhang, W.; Zhang, L.; Tellam, J.; Sougrat, R.; Laquai, F.; DeLongchamp, D. M.; Durrant, J. R.; McCulloch, I. Enhanced Photocatalytic Hydrogen Evolution from Organic Semiconductor Heterojunction Nanoparticles. *Nat. Mater.* **2020**, *19* (5), 559–565. DOI: 10.1038/s41563-019-0591-1.

(33) Cai, G.; Li, Y.; Fu, Y.; Yang, H.; Mei, L.; Nie, Z.; Li, T.; Liu, H.; Ke, Y.; Wang, X.-L.; Brédas, J.-L.; Tang, M.-C.; Chen, X.; Zhan, X.; Lu, X. Deuteration-Enhanced Neutron Contrasts to Probe Amorphous Domain Sizes in Organic Photovoltaic Bulk Heterojunction Films. *Nat. Commun.* **2024**, *15* (1), 2784. DOI: 10.1038/s41467-024-47052-7.

(34) Kilbride, R. C.; Spooner, E. L. K.; Burg, S. L.; Oliveira, B. L.; Charas, A.; Bernardo, G.; Dalgliesh, R.; King, S.; Lidzey, D. G.; Jones, R. A. L.; Parnell, A. J. The Nanoscale Structure and Stability of Organic Photovoltaic Blends Processed with Solvent Additives. *Small* **2024**, *20* (33), DOI: 10.1002/smll.202311109.

(35) Tress, W. *Organic Solar Cells: Theory, Experiment, and Device Simulation*; Springer International Publishing: Cham, 2014; pp 359–376. DOI: 10.1007/978-3-319-10097-5_7.

(36) Finck, B. Y.; Schwartz, B. J. Understanding the Origin of the S-Curve in Conjugated Polymer/Fullerene Photovoltaics from Drift-Diffusion Simulations. *Appl. Phys. Lett.* **2013**, *103* (5), 053306. DOI: 10.1063/1.4817396.

(37) Tress, W.; Corvers, S.; Leo, K.; Riede, M. Investigation of Driving Forces for Charge Extraction in Organic Solar Cells: Transient Photocurrent Measurements on Solar Cells Showing S-Shaped Current–Voltage Characteristics. *Adv. Energy Mater.* **2013**, *3* (7), 873–880. DOI: 10.1002/aenm.201200931.

(38) Wang, J. C.; Ren, X. C.; Shi, S. Q.; Leung, C. W.; Chan, P. K. L. Charge Accumulation Induced S-Shape *J–V* Curves in Bilayer Heterojunction Organic Solar Cells. *Org. Electron.* **2011**, *12* (6), 880–885. DOI: 10.1016/j.orgel.2011.02.016.

(39) Tress, W.; Petrich, A.; Hummert, M.; Hein, M.; Leo, K.; Riede, M. Imbalanced Mobilities Causing S-Shaped IV Curves in Planar Heterojunction Organic Solar Cells. *Appl. Phys. Lett.* **2011**, *98* (6), 063301. DOI: 10.1063/1.3553764.

(40) Wagenpfahl, A.; Deibel, C.; Dyakonov, V. Organic Solar Cell Efficiencies Under the Aspect of Reduced Surface Recombination Velocities. *IEEE J. Sel. Top. Quantum Electron.* **2010**, *16* (6), 1759-1763. DOI: 10.1109/JSTQE.2010.2042142.

(41) Luo, S.; Huo, M.; Xue, Q.; Xie, G. Numerical Simulation of S-Shaped Current–Voltage Curves Induced by Electron Traps in Inverted Organic Photovoltaics. *Int. J. Mol. Sci.* **2022**, *23* (4), 2039. DOI: 10.3390/ijms23042039.

(42) Sundqvist, A.; Sandberg, O. J.; Nyman, M.; Smått, J.-H.; Österbacka, R. Origin of the S-Shaped JV Curve and the Light-Soaking Issue in Inverted Organic Solar Cells. *Adv. Energy Mater.* **2016**, *6* (6), 1502265. DOI: 10.1002/aenm.201502265.

(43) Tress, W.; Inganäs, O. Simple Experimental Test to Distinguish Extraction and Injection Barriers at the Electrodes of (Organic) Solar Cells with S-Shaped Current–Voltage Characteristics. *Sol. Energy Mater. Sol. Cells* **2013**, *117*, 599–603. DOI: 10.1016/j.solmat.2013.07.014.

(44) Wang, J. C.; Ren, X. C.; Shi, S. Q.; Leung, C. W.; Chan, P. K. L. Charge Accumulation Induced S-Shape *J–V* Curves in Bilayer Heterojunction Organic Solar Cells. *Org. Electron.* **2011**, *12* (6), 880–885. DOI: 10.1016/j.orgel.2011.02.016.

(45) Kilbride, R. C.; Spooner, E. L. K.; Cassella, E. J.; O'Kane, M. E.; Doudin, K.; Lidzey, D. G.; Jones, R.; Parnell, A. J. Exploring the Impact of 1,8-Diioodoctane on the Photostability of Organic Photovoltaics. *ACS Appl. Energy Mater.* **2024**, *7* (19), 8401–8411. DOI: 10.1021/acsaem.4c01272.

(46) Hedley, G. J.; Ward, A. J.; Alekseev, A.; Howells, C. T.; Martins, E. R.; Serrano, L. A.; Cooke, G.; Ruseckas, A.; Samuel, I. D. W. Determining the Optimum Morphology in High-Performance Polymer-Fullerene Organic Photovoltaic Cells. *Nat. Commun.* **2013**, *4* (1), 2867. DOI: 10.1038/ncomms3867.

(47) Zarrabi, N.; Yazmaciyan, A.; Meredith, P.; Kassal, I.; Armin, A. Anomalous Exciton Quenching in Organic Semiconductors in the Low-Yield Limit. *J. Phys. Chem. Lett.* **2018**, *9* (20), 6144–6148. DOI: 10.1021/acs.jpclett.8b02484.

(48) D. Dimitrov, S.; Huang, Z.; Deledalle, F.; B. Nielsen, C.; C. Schroeder, B.; Shahid Ashraf, R.; Shoaee, S.; McCulloch, I.; R. Durrant, J. Towards Optimisation of Photocurrent from Fullerene Excitons in Organic Solar Cells. *Energy Environ. Sci.* **2014**, *7* (3), 1037–1043. DOI: 10.1039/C3EE42607F.

(49) Mikhnenko, O. V.; Blom, P. W. M.; Nguyen, T.-Q. Exciton Diffusion in Organic Semiconductors. *Energy Environ. Sci.* **2015**, *8* (7), 1867–1888. DOI: 10.1039/C5EE00925A.

(50) Firdaus, Y.; Le Corre, V. M.; Karuthedath, S.; Liu, W.; Markina, A.; Huang, W.; Chattopadhyay, S.; Nahid, M. M.; Nugraha, M. I.; Lin, Y.; Seitkhan, A.; Basu, A.; Zhang, W.; McCulloch, I.; Ade, H.; Labram, J.; Laquai, F.; Andrienko, D.; Koster, L. J. A.; Anthopoulos, T. D. Long-Range Exciton Diffusion in Molecular Non-Fullerene Acceptors. *Nat. Commun.* **2020**, *11* (1), 5220. DOI: 10.1038/s41467-020-19029-9.

(51) Zhang, T.; Dement, D. B.; Ferry, V. E.; Holmes, R. J. Intrinsic Measurements of Exciton Transport in Photovoltaic Cells. *Nat. Commun.* **2019**, *10* (1), 1156. DOI: 10.1038/s41467-019-09062-8.

(52) Menke, S. M.; Holmes, R. J. Exciton Diffusion in Organic Photovoltaic Cells. *Energy Environ. Sci.* **2014**, *7* (2), 499–512. DOI: 10.1039/C3EE42444H.

(53) Lunt, R. R.; Giebink, N. C.; Belak, A. A.; Benziger, J. B.; Forrest, S. R. Exciton Diffusion Lengths of Organic Semiconductor Thin Films Measured by Spectrally Resolved Photoluminescence Quenching. *J. Appl. Phys.* **2009**, *105* (5), 053711. DOI: 10.1063/1.3079797.

(54) Lee, T. H.; Park, S. Y.; Park, W.-W.; Du, X.; Son, J. H.; Li, N.; Kwon, O.-H.; Woo, H. Y.; Brabec, C. J.; Kim, J. Y. Efficient Exciton Diffusion in Organic Bilayer Heterojunctions with Nonfullerene Small Molecular Acceptors. *ACS Energy Lett.* **2020**, *5* (5), 1628–1635. DOI: 10.1021/acsenergylett.0c00564.

(55) T. Sajjad, M.; Ruseckas, A.; Krishnan Jagadamma, L.; Zhang, Y.; W. Samuel, I. D. Long-Range Exciton Diffusion in Non-Fullerene Acceptors and Coarse Bulk Heterojunctions Enable Highly Efficient Organic Photovoltaics. *J. Mater. Chem. A* **2020**, *8* (31), 15687–15694. DOI: 10.1039/D0TA06017H.

(56) Firdaus, Y.; Le Corre, V. M.; Karuthedath, S.; Liu, W.; Markina, A.; Huang, W.; Chattopadhyay, S.; Nahid, M. M.; Nugraha, M. I.; Lin, Y.; Seitkhan, A.; Basu, A.; Zhang, W.; McCulloch, I.; Ade, H.; Labram, J.; Laquai, F.; Andrienko, D.; Koster, L. J. A.; Anthopoulos, T. D. Long-Range Exciton Diffusion in Molecular Non-Fullerene Acceptors. *Nat. Commun.* **2020**, *11* (1), 5220. DOI: 10.1038/s41467-020-19029-9.

(57) Li, Q.; Wang, L.-M.; Liu, S.; Zhan, X.; Zhu, T.; Cao, Z.; Lai, H.; Zhao, J.; Cai, Y.; Xie, W.; Huang, F. Impact of Donor–Acceptor Interaction and Solvent Additive on the Vertical Composition Distribution of Bulk Heterojunction Polymer Solar Cells. *ACS Appl. Mater. Interfaces* **2019**, *11* (49), 45979–45990. DOI: 10.1021/acsami.9b15753.

(58) Wang, L-M.; Li, Q.; Liu, S.; Cao, Z.; Cai, Y-P.; Jiao, X.; Lai, H.; Xie, W.; Zhan, X.; Zhu, T. Quantitative Determination of the Vertical Segregation and Molecular Ordering of PBDB-T/ITIC Blend Films with Solvent Additives. *ACS Appl. Mater. Interfaces* **2020**, *12* (21), 24165-24173. DOI: 10.1021/acsami.0c02843.

(59) Song, X.; Gasparini, N.; Baran, D. The Influence of Solvent Additive on Polymer Solar Cells Employing Fullerene and Non-Fullerene Acceptors. *Adv. Electron. Mater.* **2018**, *4* (10), 1700358. DOI: 10.1002/aelm.201700358.

(60) MacKenzie, R. C. I.; Göritz, A.; Greedy, S.; von Hauff, E.; Nelson, J. Theory of Stark Spectroscopy Transients from Thin Film Organic Semiconducting Devices. *Phys. Rev. B* **2014**, *89* (19), 195307. DOI: 10.1103/PhysRevB.89.195307.

(61) Wang, C.; Li, C.; Wen, S.; Ma, P.; Liu, Y.; MacKenzie, R. C. I.; Tian, W.; Ruan, S. Combining Plasmonic Trap Filling and Optical Backscattering for Highly Efficient Third Generation Solar Cells. *J. Mater. Chem. A* **2017**, *5* (8), 3995–4002. DOI: 10.1039/C7TA00229G.

(62) Kan, Z.; Colella, L.; Canesi, E. V.; Vorobiev, A.; Skrypnychuk, V.; Terraneo, G.; Barbero, D. R.; Bertarelli, C.; MacKenzie, R. C. I.; Keivanidis, P. E. Charge Transport Control via Polymer Polymorph Modulation in Ternary Organic Photovoltaic Composites. *J. Mater. Chem. A* **2016**, *4* (4), 1195–1201. DOI: 10.1039/C5TA08120C.

(63) MacKenzie, R. C. I.; Balderrama, V. S.; Schmeisser, S.; Stoof, R.; Greedy, S.; Pallarès, J.; Marsal, L. F.; Chanaewa, A.; von Hauff, E. Loss Mechanisms in High Efficiency Polymer Solar Cells. *Adv. Energy Mater.* **2016**, *6* (4), 1501742. DOI: 10.1002/aenm.201501742.

(64) Tremolet de Villers, B. J.; MacKenzie, R. C. I.; Jasieniak, J. J.; Treat, N. D.; Chabinyc, M. L. Linking Vertical Bulk-Heterojunction Composition and Transient Photocurrent Dynamics in Organic Solar Cells with Solution-Processed MoO Contact Layers. *Adv. Energy Mater.* **2014**, *4* (5), 1301290. DOI: 10.1002/aenm.201301290.

(65) Doumon, N. Y.; Dryzhov, M. V.; Houard, F. V.; Le Corre, V. M.; Rahimi Chatri, A.; Christodoulis, P.; Koster, L. J. A. Photostability of Fullerene and Non-Fullerene Polymer Solar Cells: The Role of the Acceptor. *ACS Appl. Mater. Interfaces* **2019**, *11* (8), 8310–8318. DOI: 10.1021/acsami.8b20493

(66) Ding, X.; Ding, Y.-F.; Huang, C.; Li, Y.; Zhang, M.; Zhu, C.; Li, Z. Non-Covalent Interaction Enhancement on Active/Interfacial Layers via Two-Dimensional Vermiculite Doping for Efficient Organic Solar Cells. *Small* **2024**, *20* (30), 2311715. DOI: 10.1002/smll.202311715.

(67) Saerbeck, T.; Cubitt, R.; Wildes, A.; Manzin, G.; Andersen, K. H.; Gutfreund, P. Recent Upgrades of the Neutron Reflectometer D17 at ILL. *J. Appl. Crystallogr.* **2018**, *51* (2), 249–256. DOI: 10.1107/S160057671800239X.

(68) Gutfreund, P.; Saerbeck, T.; Gonzalez, M. A.; Pellegrini, E.; Laver, M.; Dewhurst, C.; Cubitt, R. Towards Generalized Data Reduction on a Chopper-Based Time-of-Flight Neutron Reflectometer. *J. Appl. Crystallogr.* **2018**, *51* (3), 606–615. DOI: 10.1107/S160057671800448X.

(69) Glavic, A.; Björck, M. GenX 3: The Latest Generation of an Established Tool. *J. Appl. Crystallogr.* **2022**, *55* (4), 1063–1071. DOI: 10.1107/S1600576722006653.

(70) Hamada, F.; Saeki, A. Mobility Relaxation of Holes and Electrons in Polymer:Fullerene and Polymer : Non-Fullerene Acceptor Solar Cells. *ChemSusChem* **2021**, *14* (17), 3528–3534. DOI: 10.1002/cssc.202100566.

ToC Graphic

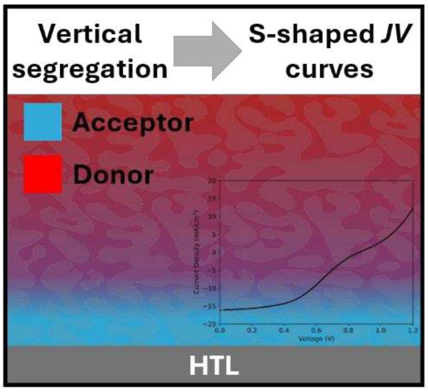

Vertical segregation
S-shaped *JV* curves
🟦 Acceptor
🟥 Donor
Current Density (mA/cm²)
20
15
10
5
0
−5
−10
−15
−20
0.0
0.2
0.4
0.6
0.8
1.0
1.2
Voltage (V)
HTL